Supplementary Material

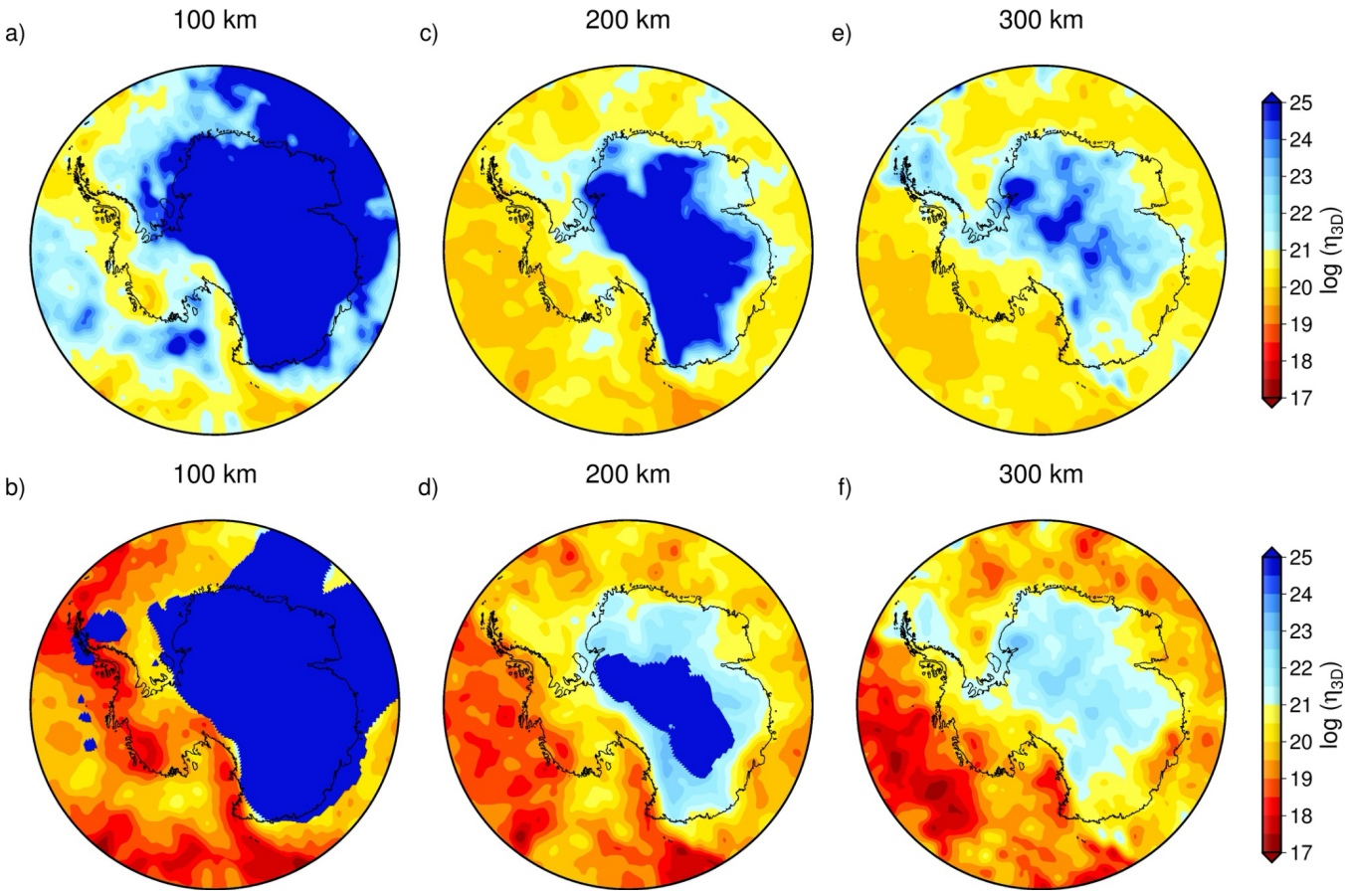

Figure S1. Earth structure for Seakon coupled simulations. Viscosity depth slices of the (a-c) primary Earth model and the (d-f) alternative Earth model. The saturated blue regions correspond to the lithosphere at the plotted depth slice.

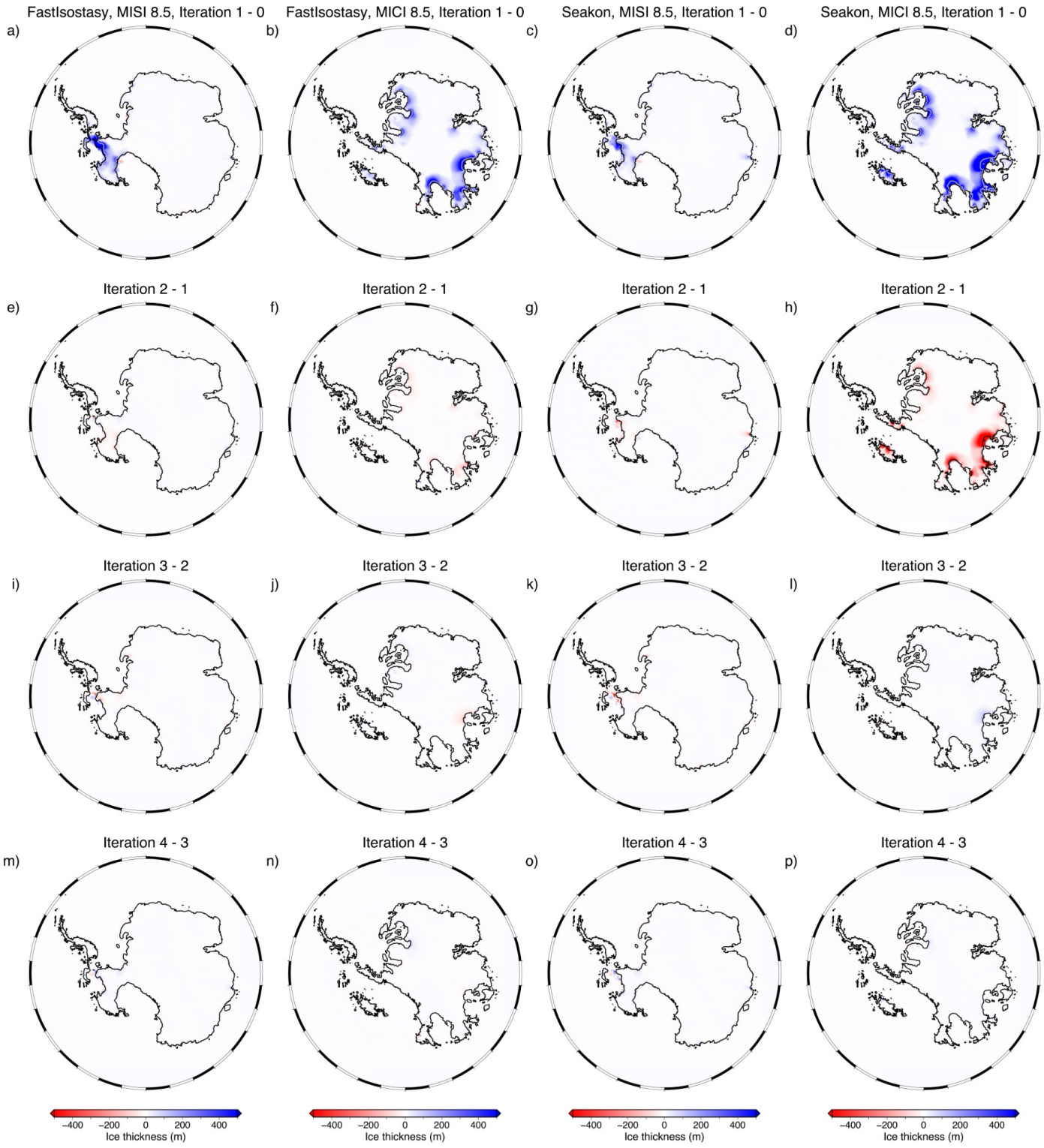

Figure S2. Difference of ice thickness at 2500 between iterations with the strong Earth model to demonstrate coupled model convergence for the weak Earth model. Each row shows the difference in ice thickness compared to the previous iteration in coupled simulations adopting FastIsostasy (first two columns) and Seakon (last two columns) for RCP-MISI8.5 and RCP-MICI8.5. To show the difference in grounding line position between iterations, the grounding line at the n iteration is plotted in black while the grounding line at the n-1 iteration is plotted in gray.

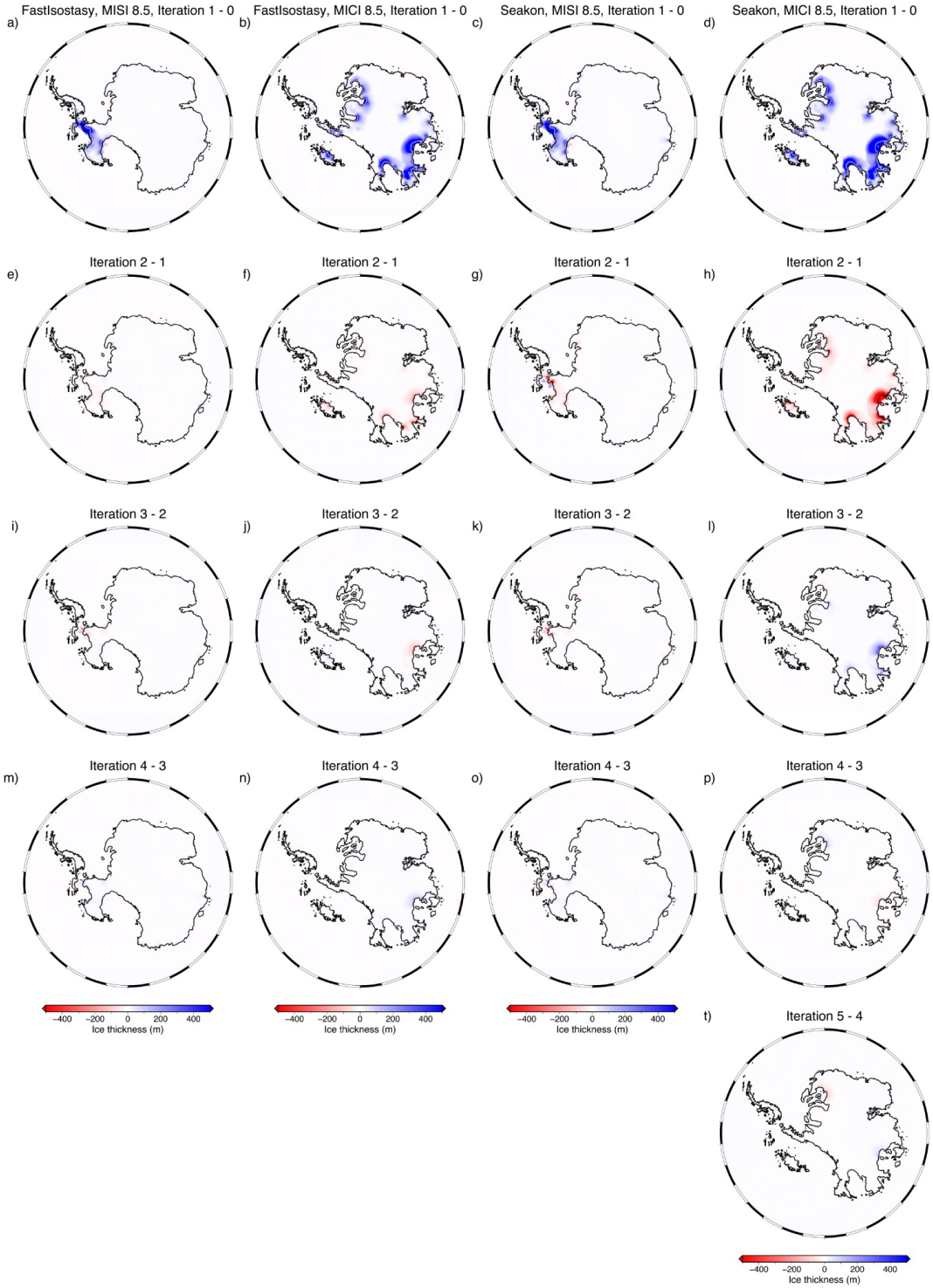

Figure S3. Difference of ice thickness at 2500 between iterations with the weak Earth model to demonstrate coupled model convergence. Each row shows the difference in ice thickness compared to the previous iteration in coupled simulations adopting FastIsostasy (first two columns) and Seakon (last two columns) for RCP-MISI8.5 and RCP-MICI8.5. To show the difference in grounding line position between iterations, the grounding line at the n iteration is plotted in black while the grounding line at the n-1 iteration is plotted in gray. With the exception of panel (b) and (d), the grounding line position for the n and n-1 iterations largely overlap.

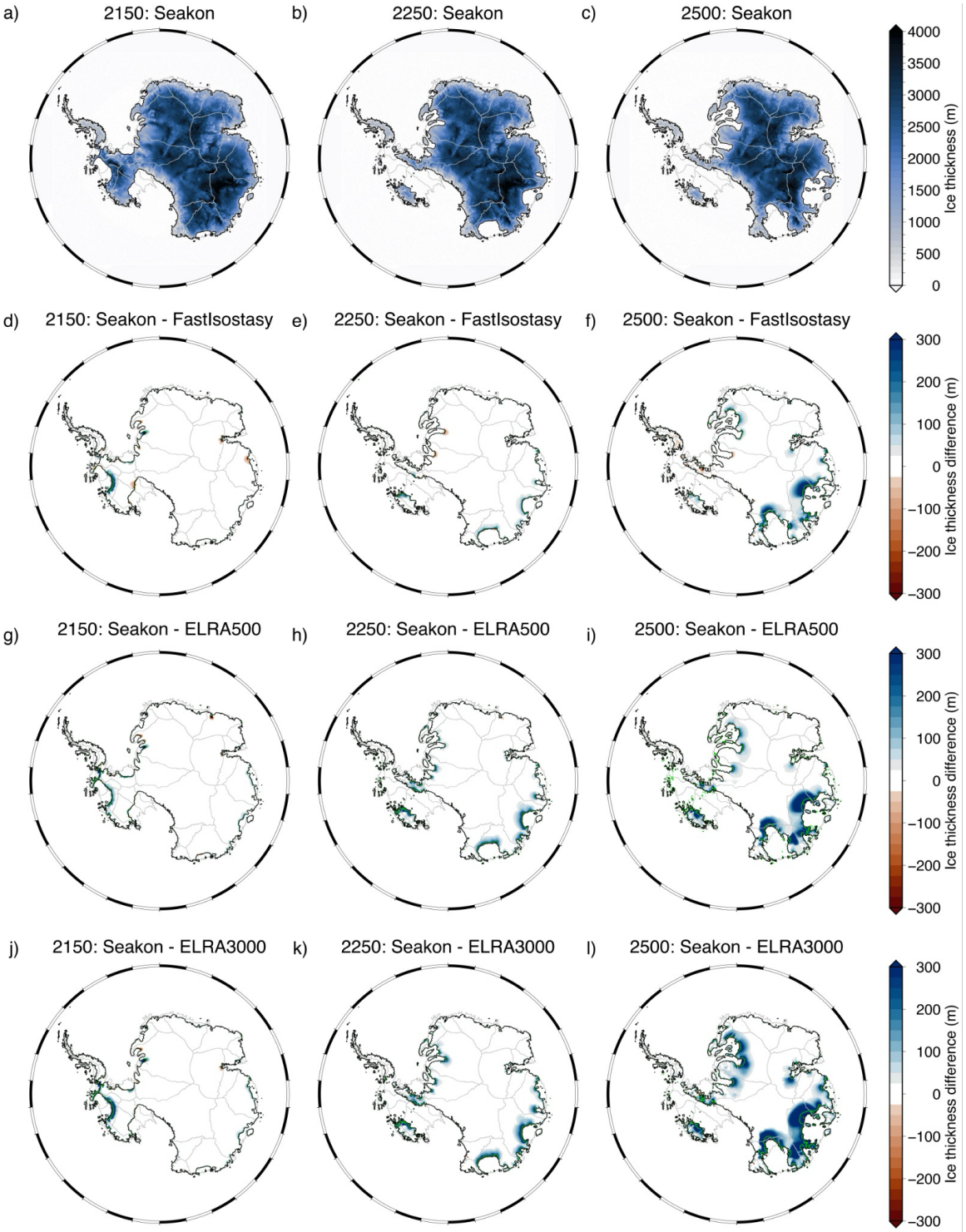

Figure S4. Ice thickness and grounding line projections for RCP-MICI8.5 from coupled Seakon and FastIsostasy simulations adopting the Weak Earth model compared with output from the ELRA simulations. (a-c) Ice thickness and grounding line (black) projections from coupled Seakon simulations for 2150, 2250, and 2500. (d-f) Ice thickness projection difference between Seakon and FastIsostasy simulations, with projected grounding lines from Seakon (black) and FastIsostasy (green). (g-i) Ice thickness differences between Seakon and ELRA500 and (j-l) between Seakon and ELRA3000, with grounding lines plotted in black (Seakon) and green (ELRA models).

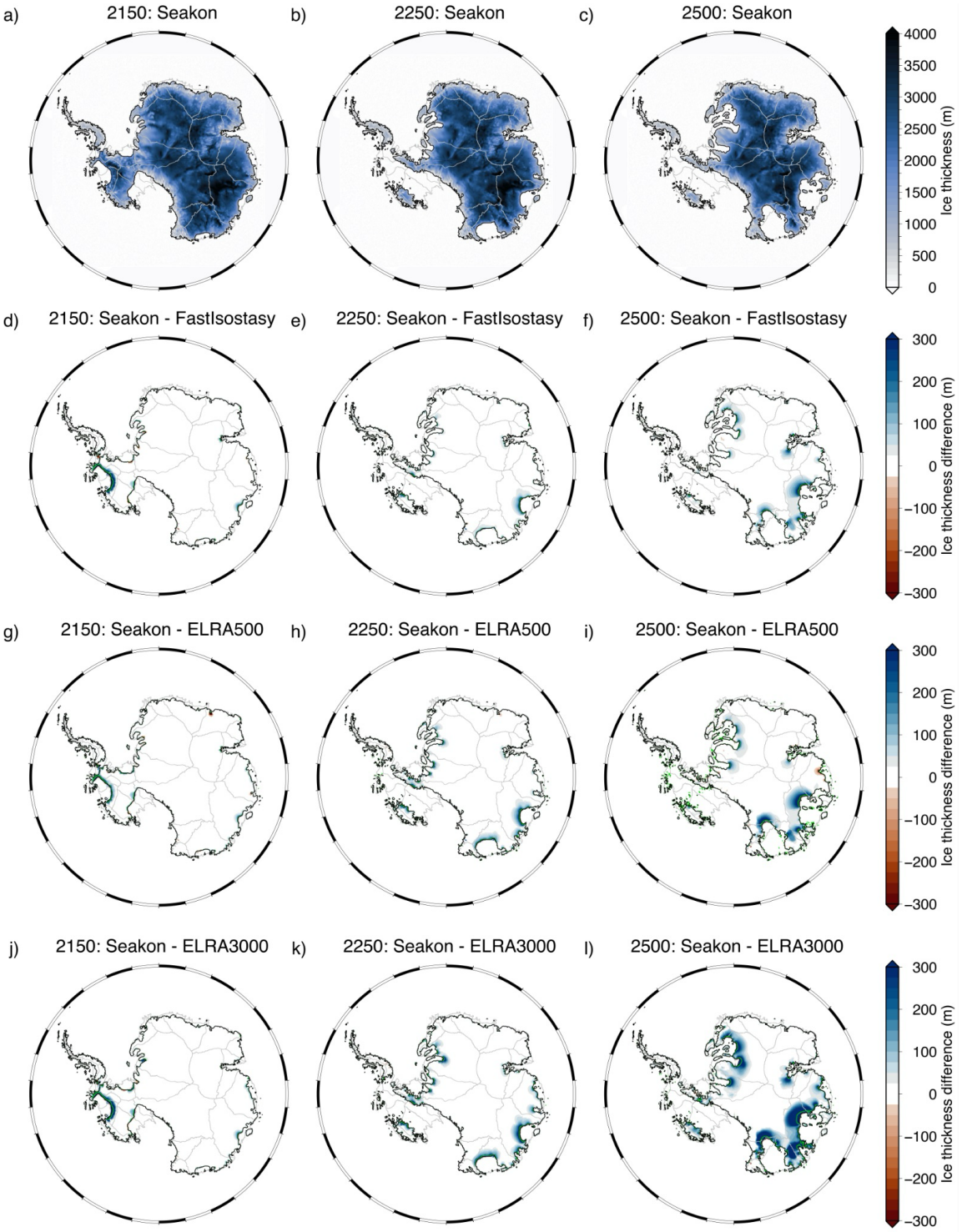

Figure S5. Ice thickness and grounding line projections for RCP-MICI8.5 from coupled Seakon and FastIsostasy simulations adopting the strong Earth model compared with output from the ELRA simulations. (a-c) Ice thickness and grounding line (black) projections from coupled Seakon simulations for 2150, 2250, and 2500. (d-f) Ice thickness projection difference between Seakon and FastIsostasy simulations, with projected grounding lines from Seakon (black) and FastIsostasy (green). (g-i) Ice thickness differences between Seakon and ELRA500 and (j-l) between Seakon and ELRA3000, with grounding lines plotted in black (Seakon) and green (ELRA models).

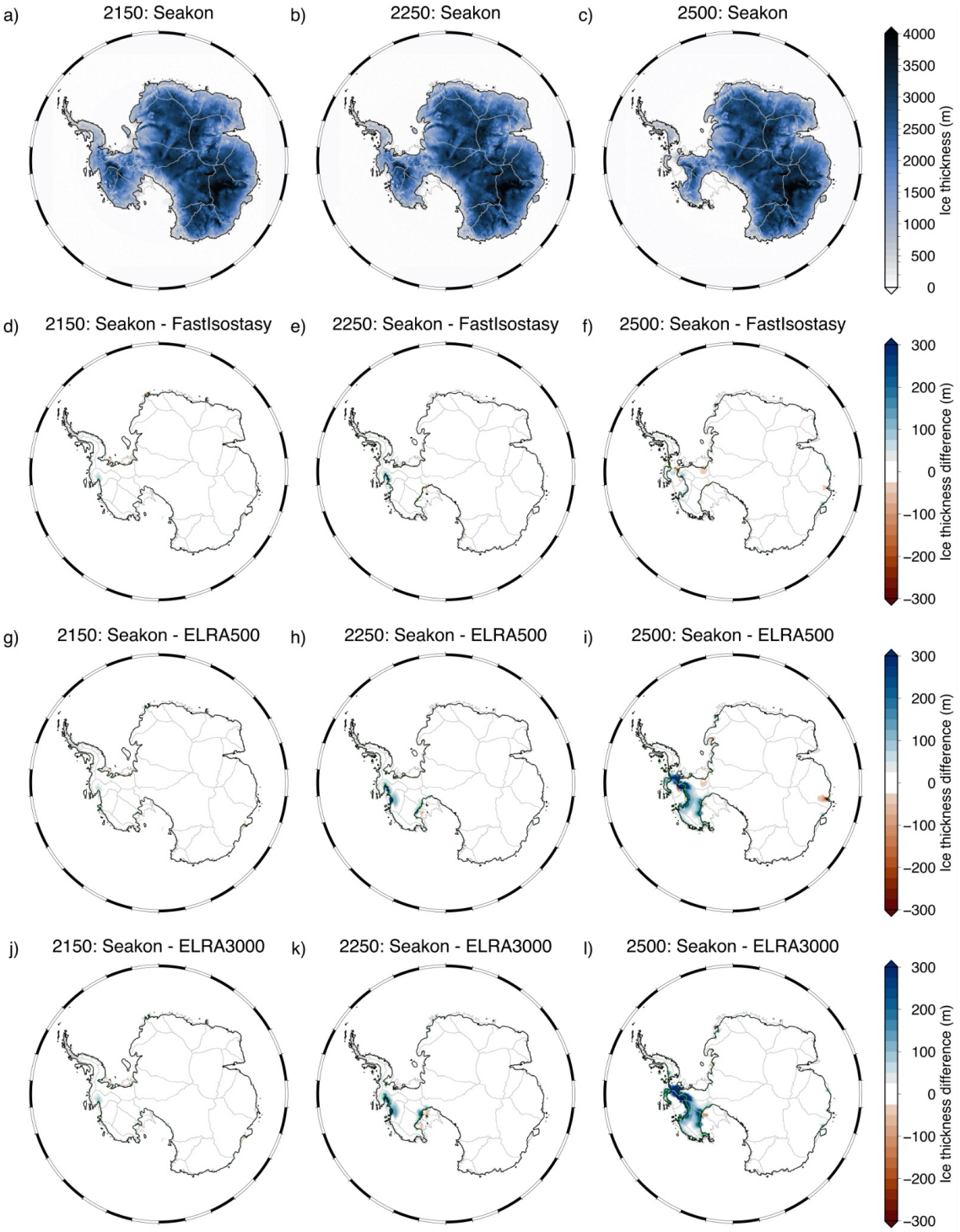

Figure S6. Ice thickness and grounding line projections for RCP-MISI8.5 from coupled Seakon and FastIsostasy simulations adopting the weak Earth model compared with output from the ELRA simulations. (a-c) Ice thickness and grounding line (black) projections from coupled Seakon simulations for 2150, 2250, and 2500. (d-f) Ice thickness projection difference between Seakon and FastIsostasy simulations, with projected grounding lines from Seakon (black) and FastIsostasy (green). (g-i) Ice thickness differences between Seakon and ELRA500 and (j-l) between Seakon and ELRA3000, with grounding lines plotted in black (Seakon) and green (ELRA models).

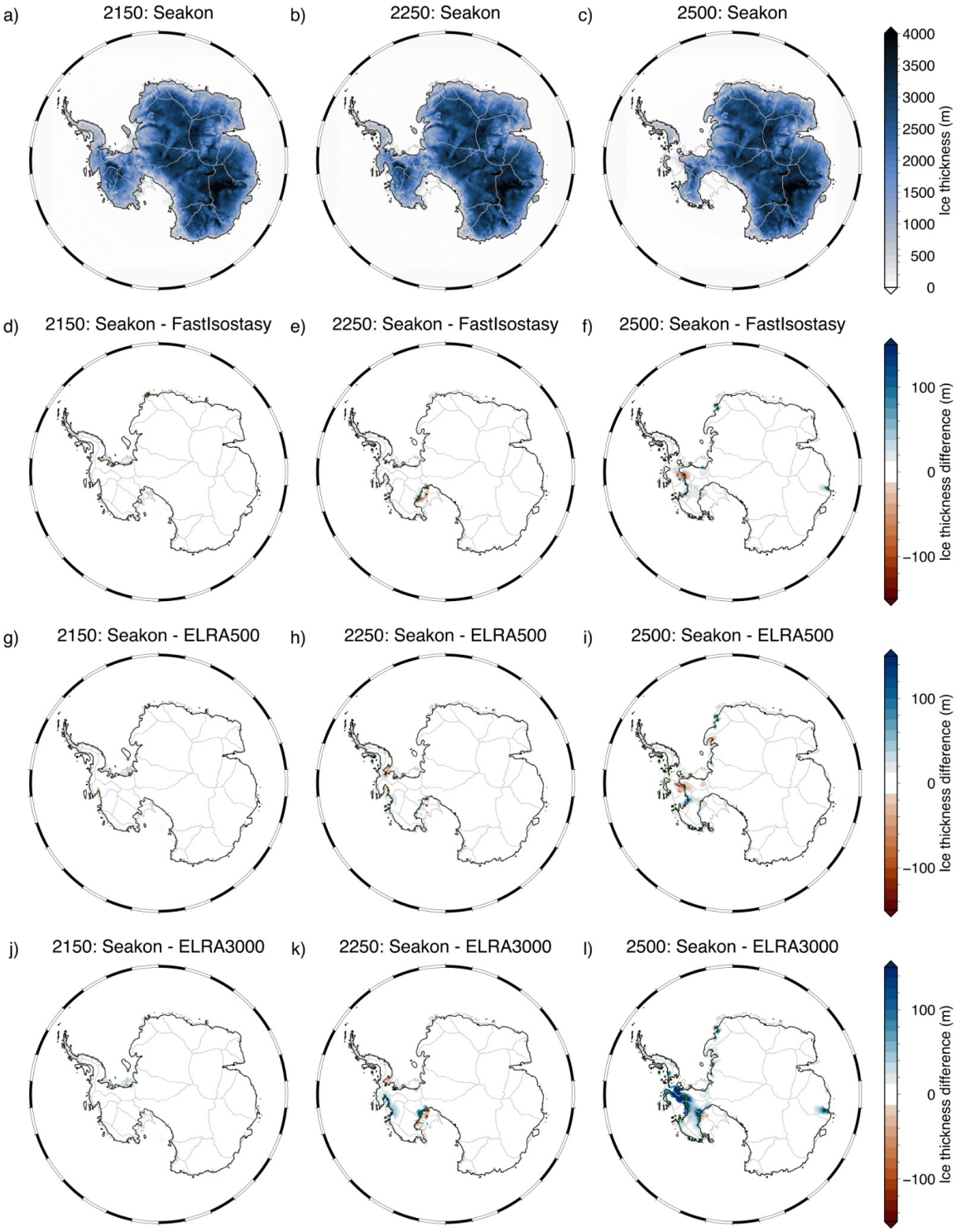

Figure S7. Ice thickness and grounding line projections for RCP-MISI8.5 from coupled Seakon and FastIsostasy simulations adopting the strong Earth model compared with output from the ELRA simulations. (a-c) Ice thickness and grounding line (black) projections from coupled Seakon simulations for 2150, 2250, and 2500. (d-f) Ice thickness projection difference between Seakon and FastIsostasy simulations, with projected grounding lines from Seakon (black) and FastIsostasy (green). (g-i) Ice thickness differences between Seakon and ELRA500 and (j-l) between Seakon and ELRA3000, with grounding lines plotted in black (Seakon) and green (ELRA models).

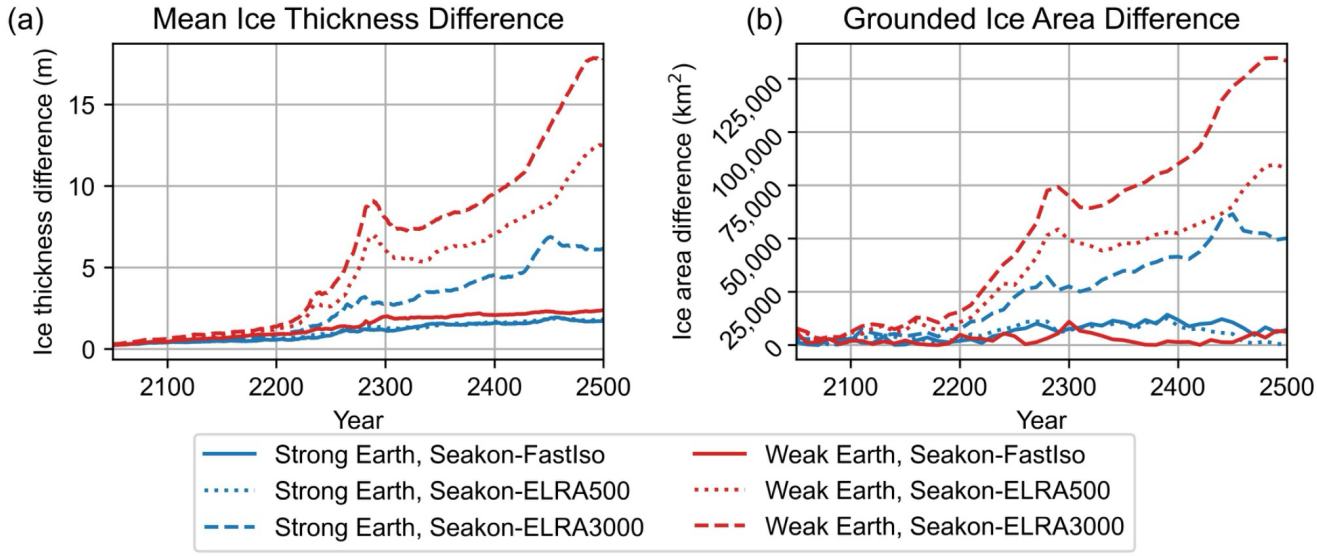

Figure S8. Difference in (a) mean grounded ice thickness and (b) grounded area extent between simulations adopting Seakon, FastIsostasy, ELRA500, and ELRA3000 for the RCP8.5-MISI scenario. Differences between the Seakon and FastIsostasy coupled simulations (Seakon-FastIso) are compared alongside differences between the Seakon and ELRA500 (Seakon-ELRA500) and Seakon and ELRA3000 (Seakon-ELRA3000) simulations.

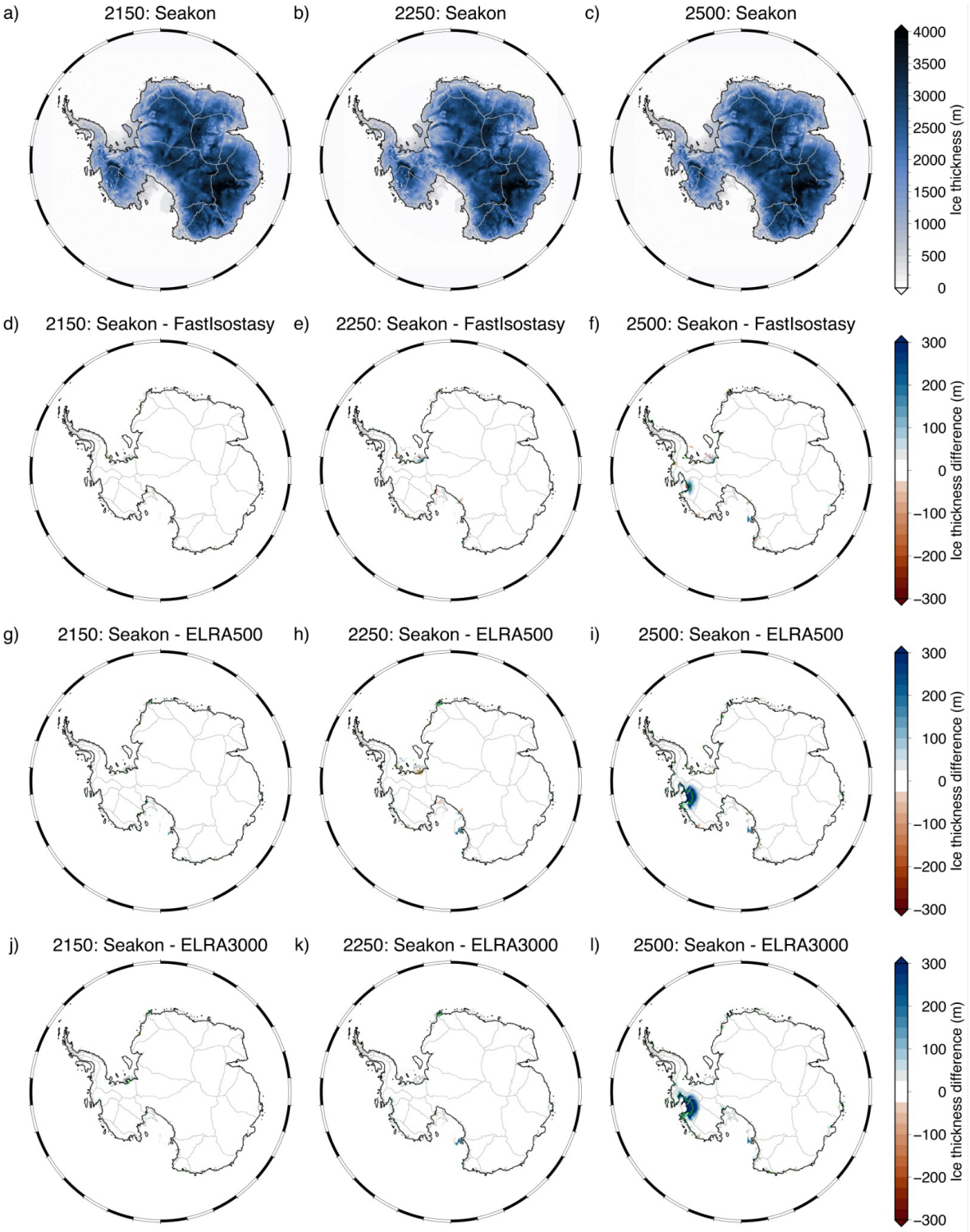

Figure S9. Ice thickness and grounding line projections for RCP-MISI2.6 from coupled Seakon and FastIsostasy simulations adopting the weak Earth model compared with output from the ELRA simulations. (a-c) Ice thickness and grounding line (black) projections from coupled Seakon simulations for 2150, 2250, and 2500. (d-f) Ice thickness projection difference between Seakon and FastIsostasy simulations, with projected grounding lines from Seakon (black) and FastIsostasy (green). (g-i) Ice thickness differences between Seakon and ELRA500 and (j-l) between Seakon and ELRA3000, with grounding lines plotted in black (Seakon) and green (ELRA models).

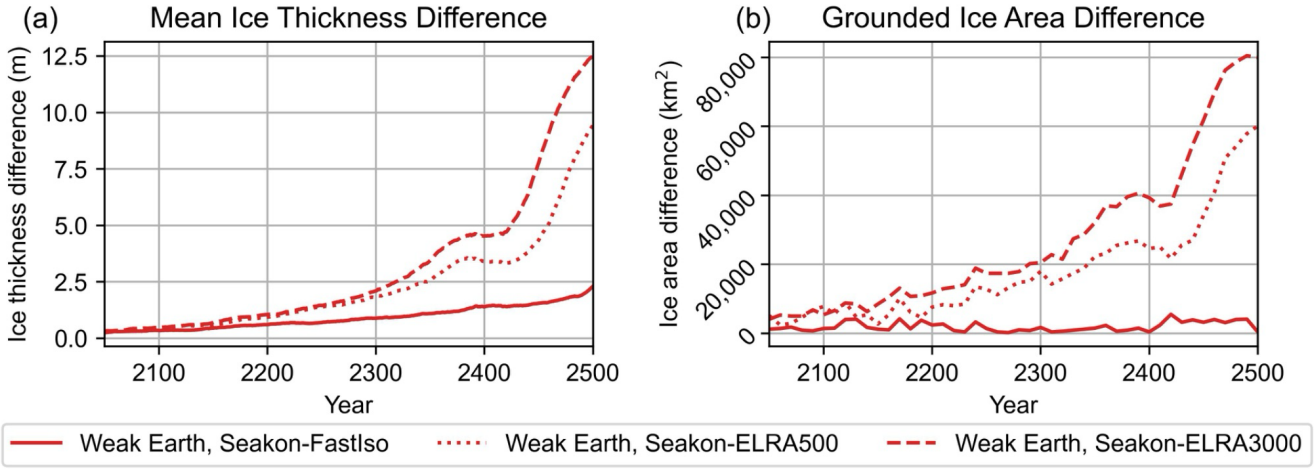

Figure S10. Difference in (a) mean grounded ice thickness and (b) grounded area extent between simulations adopting Seakon, FastIsostasy, ELRA500, and ELRA3000 for the RCP2.6-MISI scenario with the weak Earth model. Differences between the Seakon and FastIsostasy coupled simulations (Seakon-FastIso) are compared alongside differences between the Seakon and ELRA500 (Seakon-ELRA500) and Seakon and ELRA3000 (Seakon-ELRA3000) simulations.

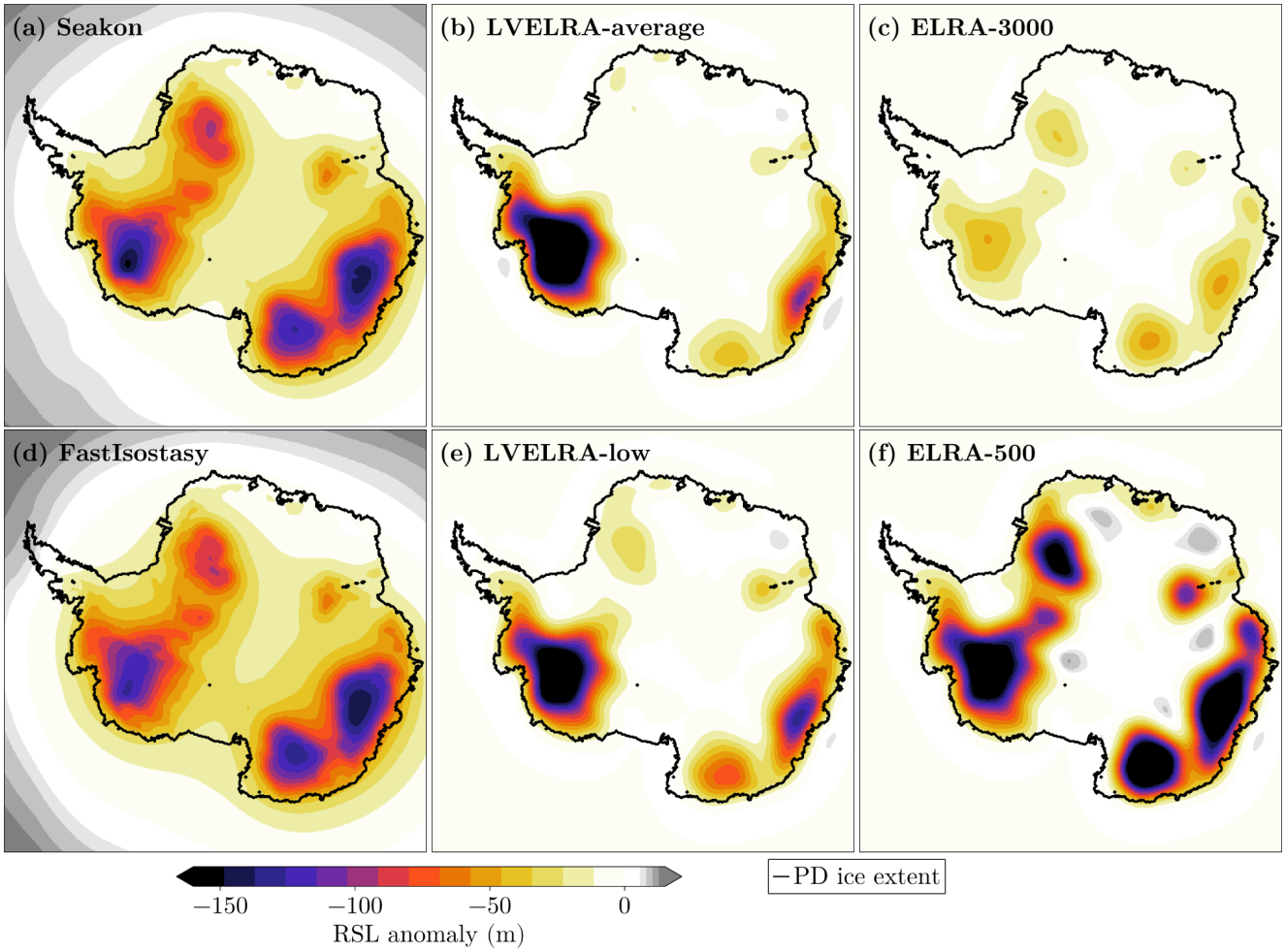

Fig. S11. Relative sea level (RSL) anomaly with respect to year 1950 for various GIA models under RCP8.5-MICI. For Seakon, FastIsostasy and LV-ELRA, the solid-Earth parameters are derived from the strong Earth model.

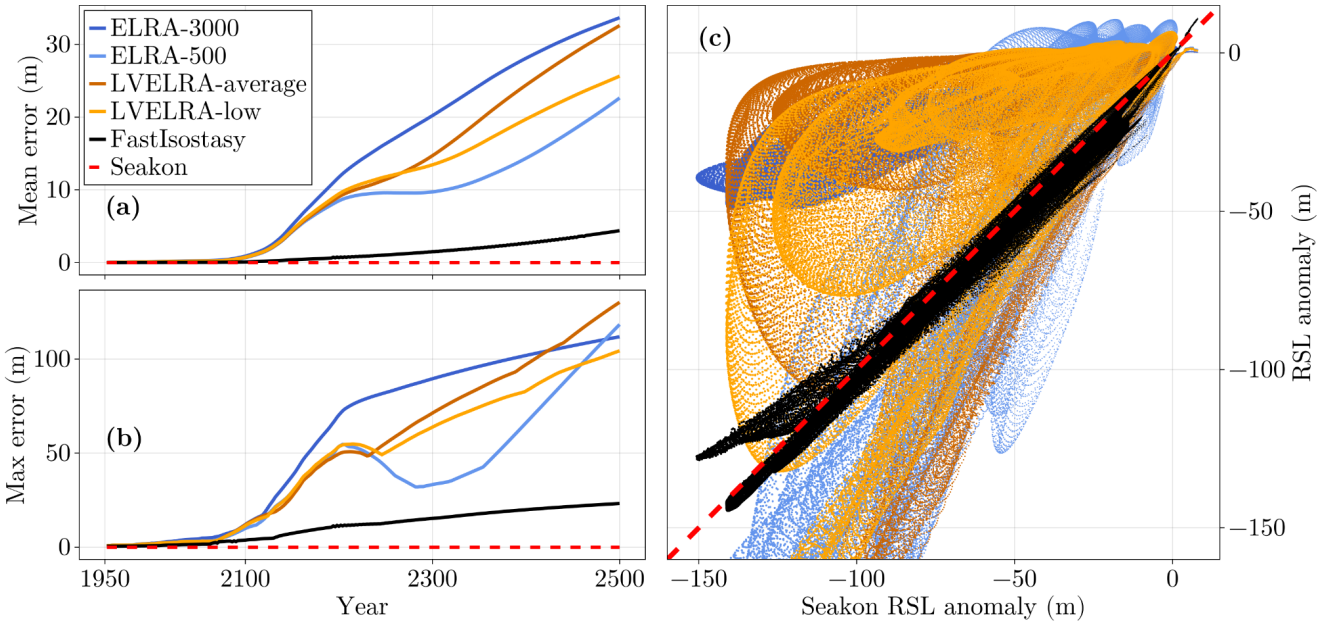

Fig. S12. (a-b) Transient evolution of the mean and maximal error in absolute RSL anomaly with respect to Seakon for simulations with the strong Earth model under RCP8.5-MICI. (c) Error plot of the RSL anomaly. For Seakon, FastIsostasy and LV-ELRA, the solid-Earth parameters are derived from the strong Earth model.

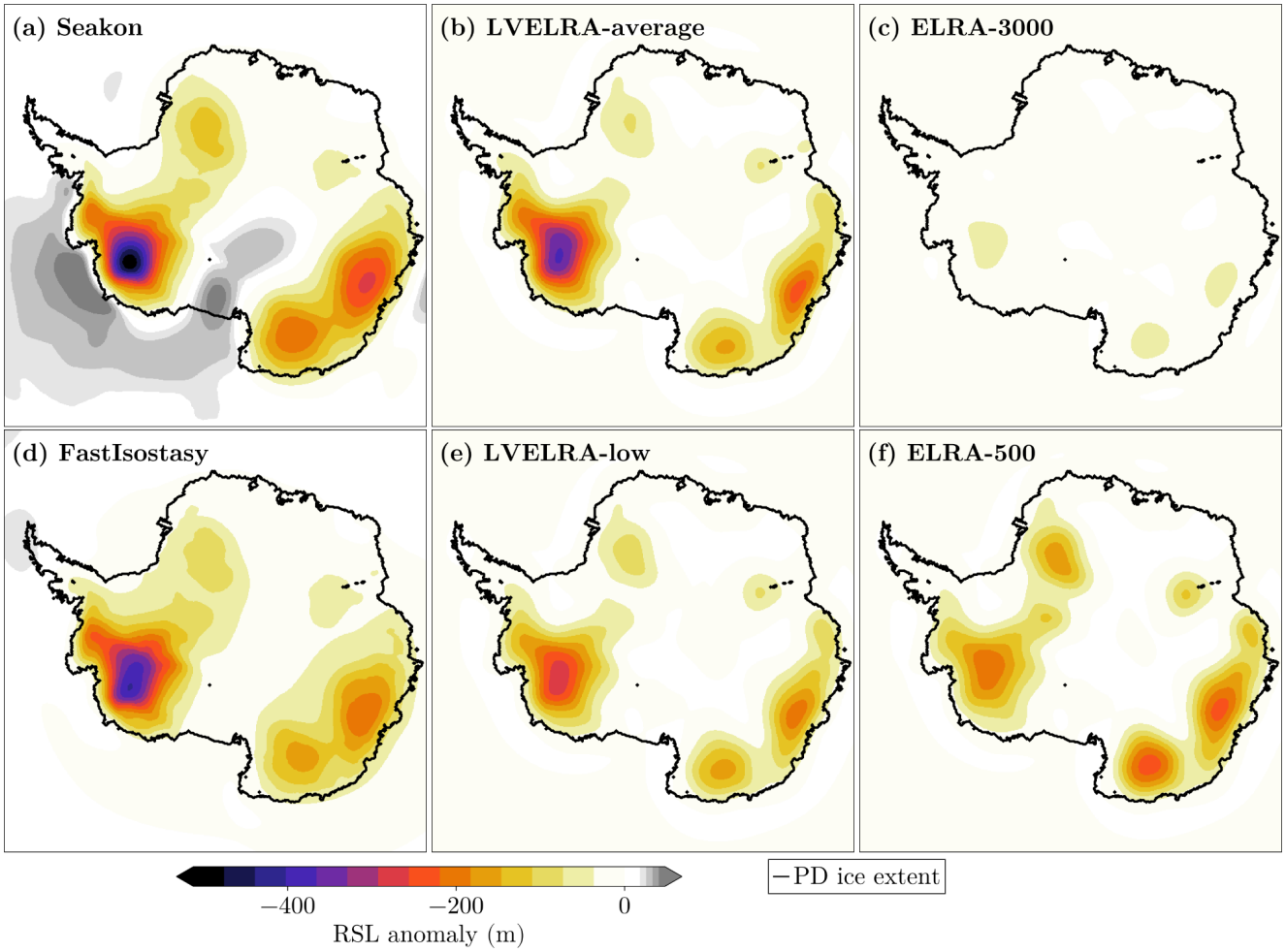

Fig S13. RSL anomaly with respect to the year 1950 for various GIA models under RCP8.5-MICI. For Seakon, FastIsostasy and LV-ELRA, the solid-Earth parameters are derived from the weak Earth model.

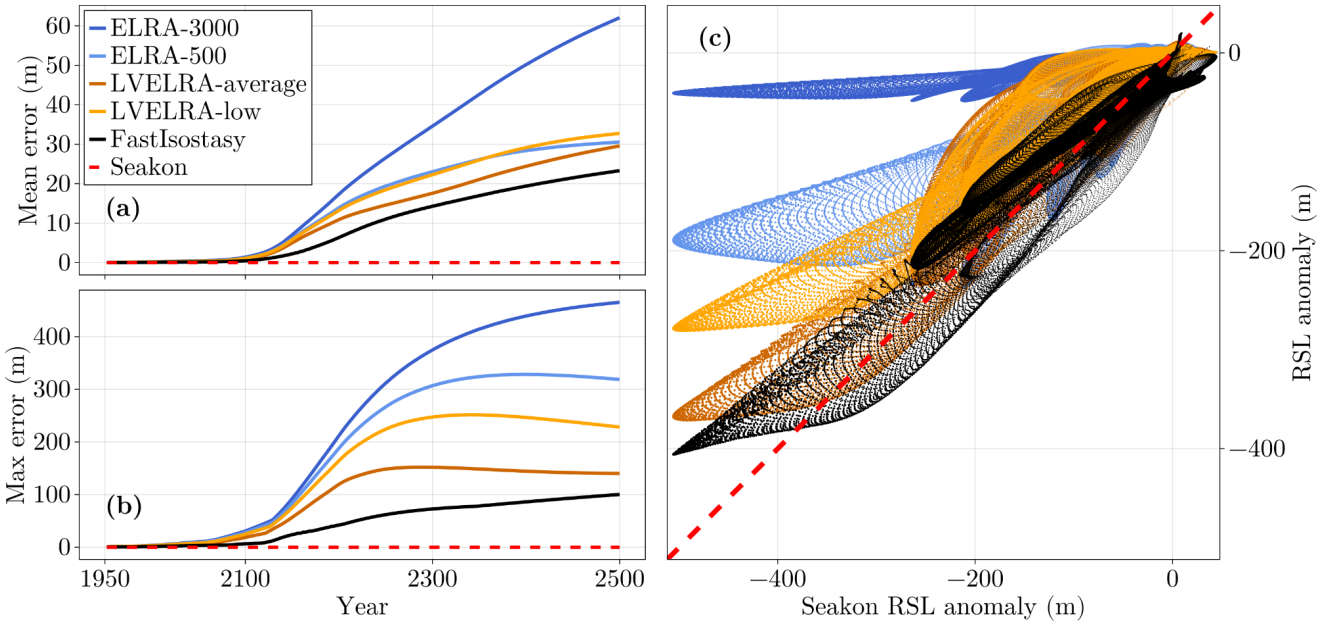

Fig S14. (a-b) Transient evolution of the mean and maximal error in absolute RSL anomaly with respect to Seakon under RCP8.5-MICI. (c) Error plot of the RSL anomaly. For Seakon, FastIsostasy and LV-ELRA, the solid-Earth parameters are derived from the weak Earth model.

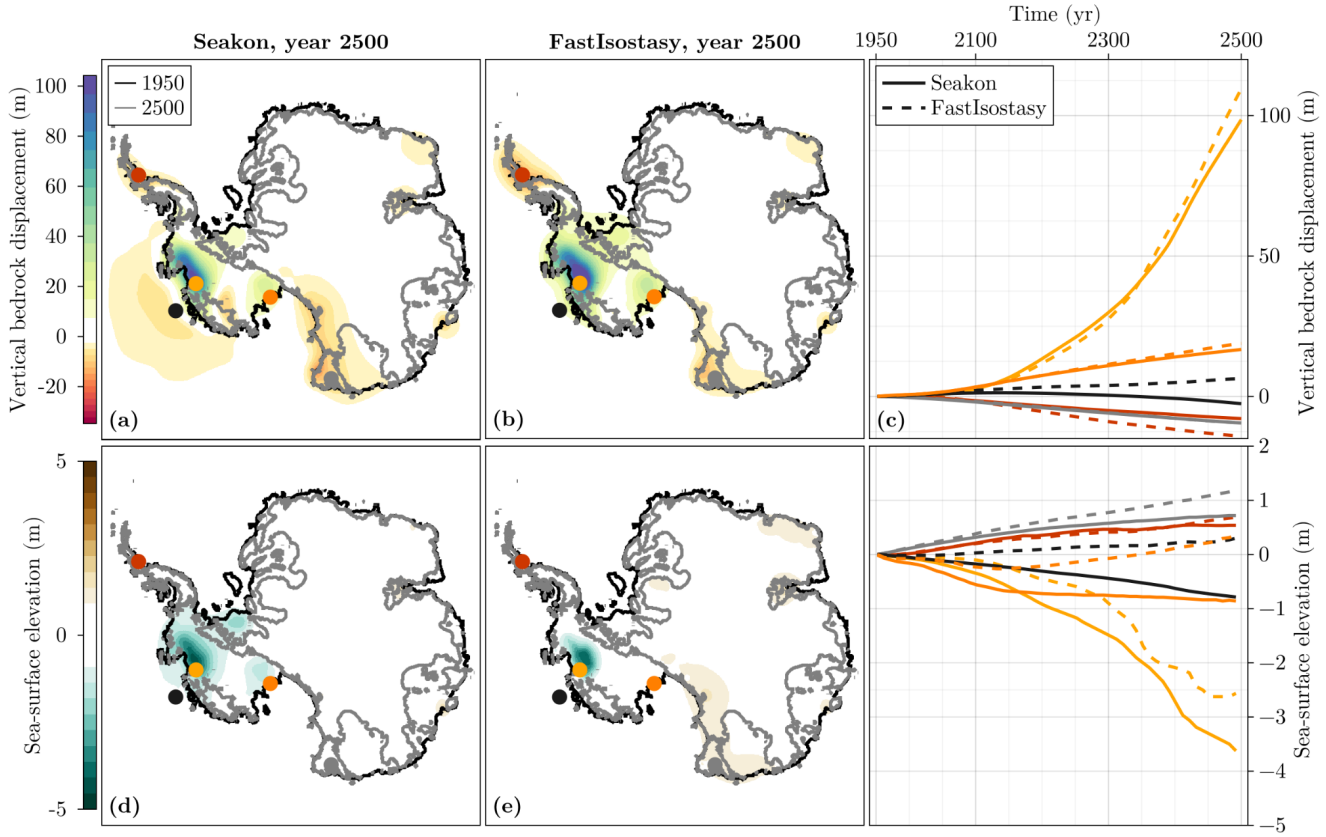

Fig. S15. (a-c) Vertical bedrock displacement and (d-f) sea-surface elevation of Seakon and FastIsostasy for the strong Earth model and RCP2.6.